MAGNETISM

Large effective magnetic fields from chiral phonons in rare-earth halides

Jiaming Luo[1,2], Tong Lin[1], Junjie Zhang[1], Xiaotong Chen[1], Elizabeth R. Blackert[1], Rui Xu[1], Boris I. Yakobson[1], Hanyu Zhu[1]*

Time-reversal symmetry (TRS) is pivotal for materials' optical, magnetic, topological, and transport properties. Chiral phonons, characterized by atoms rotating unidirectionally around their equilibrium positions, generate dynamic lattice structures that break TRS. Here, we report that coherent chiral phonons, driven by circularly polarized terahertz light pulses, polarize the paramagnetic spins in cerium fluoride in a manner similar to that of a quasi-static magnetic field on the order of 1 tesla. Through time-resolved Faraday rotation and Kerr ellipticity, we found that the transient magnetization is only excited by pulses resonant with phonons, proportional to the angular momentum of the phonons, and growing with magnetic susceptibility at cryogenic temperatures. The observation quantitatively agrees with our spin-phonon coupling model and may enable new routes to investigating ultrafast magnetism, energy-efficient spintronics, and nonequilibrium phases of matter with broken TRS.

The term "chiral" most commonly refers to structural chirality without any mirror symmetry in three-dimensional space. Meanwhile, in condensed matter physics, "chiral" sometimes implies a lack of both mirror lines within a two-dimensional plane and time-reversal symmetry (TRS) (*1*–*5*). Chiral wave functions with broken TRS and nonzero angular momenta may have topologically protected properties, such as lossless transport of the chiral edge states in the quantum Hall effect and robust vortices in chiral superconductors. Symmetry breaking is either spontaneous or externally stimulated by magnetic fields, optical excitations, and mechanical motion, which are typically implemented globally on a macroscopic scale (*6*, *7*). The breaking of mechanical TRS may also be implemented at the atomic level and femtosecond time frame, when atoms are displaced away from the equilibrium position inside the lattice and rotate unidirectionally in elliptical trajectories with nonzero angular momenta (*8*–*12*). Such vibrational modes are termed chiral phonons, providing a distinctive approach to controlling the TRS of electronic and magnetic properties. Phononic TRS breaking is a correction to the standard Born-Oppenheimer approximation, which assumes frozen lattices and preserves TRS in solving electronic states. Such correction has been theoretically demonstrated by considering the ionic current (*13*, *14*), electronic Berry phase accumulation (*15*–*18*), and nonadiabatic dynamics (*19*).

Chiral phonons carrying angular momentum have been experimentally validated across multiple material systems and physical processes, including Raman scattering, ultrafast demagnetization, and the thermal Hall effect (*20*–*26*). These phonons have been found to effectively exchange angular momentum with the spin and orbital degrees of freedom (*27*). Occasionally, in materials with strong spin-phonon coupling, the observed phononic effective magnetic moments are orders of magnitude larger than those expected from the ionic loop current (*28*–*30*). Several mechanisms have been proposed to explain such an extraordinary enhancement, including bond-dependent exchange interaction, spin-orbit tilting, hybridization with orbital excitations, and ferroelectric instability (*19*, *31*–*34*). Reciprocal to the field-induced shifts in phonon frequencies, the same mechanism theoretically allows coherent chiral phonons to generate substantial effective magnetic fields inside the materials (*14*, *35*).

However, quantitative studies of phononic magnetism remain elusive because of the challenges in manipulating coherent chiral phonons. Recent advances in nonlinear phononic spectroscopy enabled mode-selective optical excitations of linearly polarized phonons, which have been shown to significantly modulate the structural, electronic, magnetic, and topological properties in many quantum materials (*36*–*40*). In particular, phonon-induced magnetic dynamics have been found by driving one or two linear phonon modes (*40*–*42*). These phonons are not chiral eigenmodes and result in either periodic or impulsive modulation to the interatomic distances, orbital symmetry, and exchange interactions, as opposed to quasi-static breaking of TRS on demand (*43*). Chiral phonons can be excited by strong, narrowband, and circularly polarized (CP) light in the terahertz (THz) frequency range from tabletop nonlinear sources and free-electron lasers. These excitations reportedly produced ionic Kerr effect and ferromagnetic switching, but the magnetic fields are rather small, estimated to be on the order of millitesla (*44*, *45*).

Chiral phonon–spin coupling in CeF_3

In this study, we quantitatively measured the quasi-static effective magnetic fields that result from chiral phonons in the paramagnetic rare-earth trihalide CeF_3. We found a field strength of >0.9 T from the infrared-active optical phonons centered around 10.5 THz, driven by CP THz pulses with a moderate incident fluence of ~0.4 mJ/cm^2. The effective magnetic field of the phonons polarizes the paramagnetic spin of the Ce^{3+} ions and is quantified by time-resolved Kerr ellipticity. The spin polarization is proportional to the angular momentum of the driving pulses and the phonons, showing the signature of a TRS-breaking dynamic structure. We proved that the sharply increasing magnetization in cryogenic temperatures correlates with the diverging paramagnetic susceptibility, along with the appearance of resonant atomic displacement that is evidenced by time-dependent second-harmonic generation, ruling out the mechanism of a pure transition between the crystal electric field (CEF) levels. From the rate equation of paramagnetic relaxation, we deduced the transient effective magnetic field that quantitatively agrees with the modeled phonon dynamics and the spin-phonon coupling Hamiltonian throughout the temperature range of 10 to 150 K. The strength of the effective magnetic field is proportional to the number of phonons and can potentially reach 50 T under experimentally feasible conditions (*46*). Our method of coherently manipulating magnetic chiral phonons may apply to a broad range of quantum materials to unravel TRS-breaking processes that involve lattice dynamics (*15*–*19*, *31*–*33*).

The magneto-phonon properties of CeF_3 are unusual (fig. S6): The doubly degenerate E_g (391 cm^{-1}) and E_u (~350 cm^{-1}) phonons split in energy when the paramagnetic spins are polarized. At low temperatures, the magnetic susceptibility χ diverges, which enhances the effective Zeeman splitting of these phonons under magnetic fields to >3 cm^{-1}/T, equivalent to a large phononic magnetic moment of >7 μ_B (Bohr magneton) at 1.9 K (*47*–*49*). This moment is about five orders of magnitude larger than what would be expected from ionic current (*13*). It does not saturate at lower temperatures and can exceed the magnetic moments of CEF levels (<2.5 μ_B), meaning that the observed splitting is not simply caused by the hybridization of phonons and CEF levels at different frequencies (*50*–*52*). Rather, a more plausible mechanism might be the spin-dependent

[1]Department of Materials Science and Nano Engineering, Rice University, Houston, TX 77005, USA. [2]Applied Physics Graduate Program, Rice University, Houston, Texas 77005, USA.
*Corresponding author. Email: hanyu.zhu@rice.edu

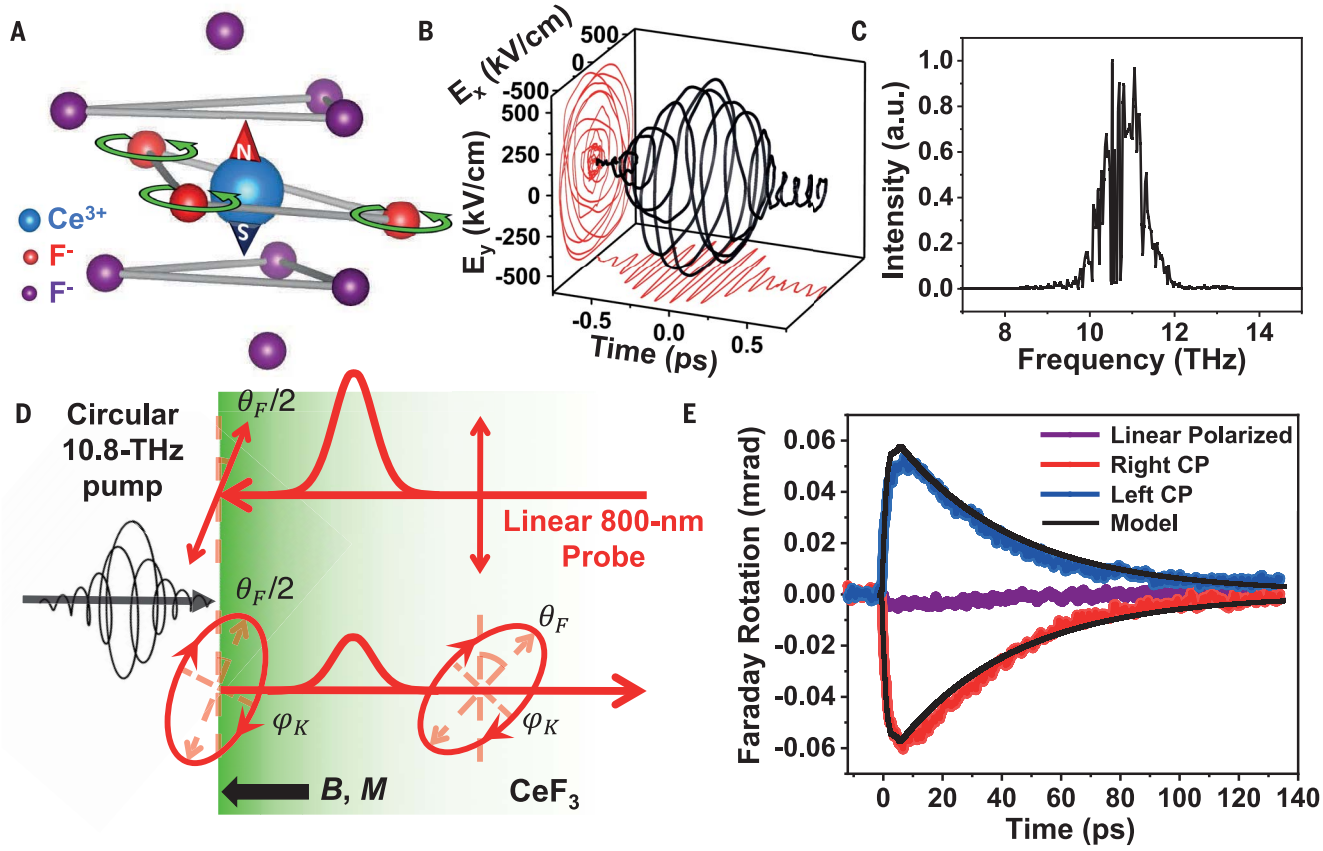

Fig. 1. Ultrafast magnetization induced by chiral phonons in CeF_3. (**A**) Illustration of part of the unit cell centered around a Ce^{3+} ion and the atomic displacement of E_u chiral phonon mode centered around 10.5 THz according to DFT calculations. The F^- ions are denoted in red and purple according to their difference in effective charge tensor. (**B**) Electric field of the CP THz pump pulse (with a helicity of 88%) as a function of time measured by electro-optic sampling. The peak field incident on the material is ~5.6 × 10^7 V/m, and the pulse duration is ~0.45 ps. (**C**) In the frequency domain, the pulse is centered at 10.8 THz with 1-THz bandwidth. (**D**) Schematic of the time-resolved Kerr ellipticity and Faraday rotation process. The CP THz pump pulses are incident from the left and exponentially decay inside the crystal, which generate an effective magnetic field perpendicular to the surface and a layer of transient magnetization (green shade) on the order of 1 μm in thickness. The linearly polarized probe with a wavelength centered at 800 nm and a duration of 0.5 ps comes from the back of the sample, experiencing twice the Faraday rotation from the magnetization layer, as well as the Kerr ellipticity from reflectance at the interface. (**E**) Faraday rotation as a function of delay time is opposite under left CP and right CP THz excitation, evidencing TRS breaking.

renormalization of phonon frequencies by nonresonant CEF (*53*), which has reproduced the order of magnitude of spin-phonon coupling in $CeCl_3$ using a simple point-charge model (*34*). Without knowing the microscopic theories, a simple phenomenological Hamiltonian under the symmetry constraint is sufficient to connect the observed phonon magnetic moment with the phonon-induced effective magnetic field: $H = K\boldsymbol{\mu} \cdot \boldsymbol{L}$, where $\boldsymbol{\mu}$ and $\boldsymbol{L}$ are the spin magnetic moment and the net angular momentum of phonons, respectively, and K is proportional to the phononic magnetic moment (*35*). When the spins are fully polarized to the saturation magnetic moment $\boldsymbol{\mu}_S$ by external fields, the frequency of a chiral phonon mode shifts by a saturation value $\Delta\Omega = 0.3 \pm 0.1$ THz. Conversely, when chiral phonons are present, the energy of the spins shifts as if influenced by an effective magnetic field [i.e., a phononic inverse Faraday effect (*54*)]:

$$B_{\text{eff}} = \frac{\hbar\Delta\Omega}{\mu_S} n \quad (1)$$

THz phonon-induced magnetization

In our experiment, we excite chiral phonons in c-cut CeF_3 by using normal-incident, resonant, and CP THz pump pulses. The doubly degenerate Raman- and infrared-active modes, which are enabled by the trigonal $\bar{P}3C1$ space group of the lattice, can both be expressed in CP basis along the c axis with a pseudo-angular momentum quantum number ±1 (table S2). Among the 12 possible pairs of chiral phonons, we chose to measure the effective magnetic field of the infrared-active, doubly degenerate phonon pairs $E_u^{\pm}$ centered around 10.5 THz, because of their large angular momentum according to density functional theory (DFT) calculations and the most prominent magnetic field–dependent infrared activity. The displacements of all six Ce^{3+} ions in the unit cell are in phase for these modes, so for clarity, we only plot a part of the unit cell in Fig. 1A. The F^- ions in the Ce^{3+} plane exhibit the largest displacement, modifying the local crystal field and mixing the CEF levels under the constraint of pseudo-angular momentum conservation. The other F^- ions are in equivalent crystallographic positions and have small displacement. The $E_u^{\pm}$ phonons are selectively and strongly coupled with CP THz photons, which are created by chirped-pulse difference frequency generation in nonlinear organic crystals and a variable phase delay between two cross-linearly polarized beams (fig. S1) (*54*). The maximum helicity of the combined THz pulses reaches ~88% (Fig. 1B and fig. S10).

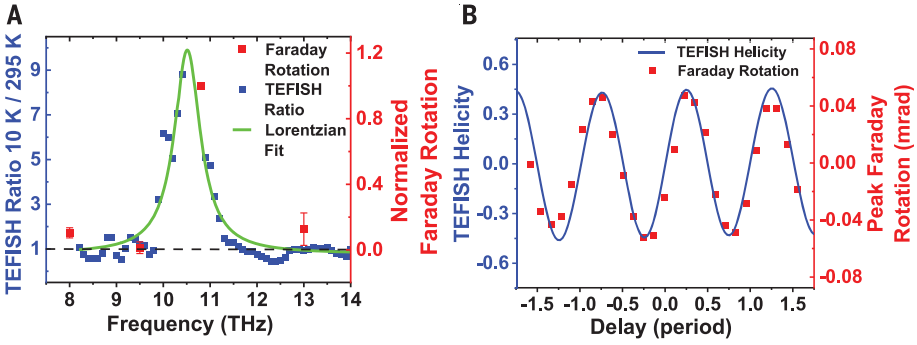

Fig. 2. Correlation between the coherent chiral phonons and the magnetization. (**A**) Ratio between the TEFISH spectra measured at 10 and 295 K. A Lorentzian fit reveals a resonant phonon peak centered around 10.5 THz. The same resonance is observed for the Faraday rotation induced by THz excitation at different frequencies, normalized by the pulse energy, confirming that the observed magnetization has a phononic origin. (**B**) Calculated helicity of the TEFISH signal and the measured peak Faraday rotation at 10 K as a function of retardation (in the unit of phononic period) between the horizontally and vertically polarized THz pump pulses, demonstrating that the magnetization arises from the angular momentum of phonons.

We then measure the phonon-induced magnetization by time-resolved magneto-optic Kerr ellipticity and Faraday rotation (Fig. 1C) (*54*). The linearly polarized near-infrared probe pulses are tightly focused onto the center of the THz pump pulses by an objective lens from the back of the sample. The pulse duration is ~0.5 ps because of the dispersion of the optics, which limits the temporal resolution, but at the same time filters out irrelevant, fast-oscillating field-induced polarization effects. The penetration depth of the THz field and the layer of magnetization is <1 μm thick, so group velocity mismatch between the pump and probe fields is negligible. Because CeF_3 is nearly lossless at the probe wavelength, the Kerr ellipticity mainly comes from the reflectance at the vacuum-sample interface, and the Faraday rotation mainly comes from transmitting through the entire layer of magnetization. The two effects happen to have comparable magnitude in our experiment and correspond to the same magnetization dynamics (figs. S4 and S8). Figure 1E shows the Faraday rotation of CeF_3 at 10 K excited by left CP, right CP, and linearly polarized THz pulses near the phonon resonance. The spin accumulation stage lasts a few picoseconds, longer than the pulse duration, and cannot be explained by the optical inverse Faraday effect or the direct optical excitation of the CEF levels. Instead, additional degrees of freedom must be present, such as phonons, magnons, or metastable states, to mediate the light-spin interaction (*39*). The magnetization switches sign for pulses with opposite helicity and approaches zero when TRS is preserved under linearly polarized excitation. The remnant signal comes from a small THz ellipticity caused by the birefringence of the diamond window. Such TRS dependence means that the magnetization dynamics is not from thermal or doping effects.

Next, we prove that coherent chiral phonons are the source of the observed magnetization by heterodyne THz electric field–induced second-harmonic generation (TEFISH) (*54*, *55*). Normally, TEFISH in thin films is dominated by atomic displacement when the THz field is resonant with the phonons (*55*). Yet in bulk crystals, the contribution from pure electric field effect is magnified by phase matching and difficult to separate from the atomic contribution at room temperature (fig. S9). Fortunately, the atomic contribution grows with the phononic coherence lifetime, which increases at cryogenic temperatures, and thus can be extracted from the temperature dependence of TEFISH in bulk CeF_3. Figure 2A shows the ratio of frequency-domain TEFISH signals measured at 10 K and room temperature. We found that the ratio is close to 1, suggesting a temperature-independent field effect, in a broad range of 8 to 14 THz except for a sharp resonance centered around 10.5 THz, which agrees with the E_u phonons measured by ellipsometry (fig. S7). Therefore, we attribute this resonant component to the atomic displacement from coherent phonons. By varying the center frequency of the THz excitation, we found that the magnetization only occurs near the phonon resonance and thus cannot be attributed to the inverse Faraday effect from the THz electric field. Furthermore, we verified that the maximum magnetization occurs at atomic displacements with almost equal amplitude in the horizontal and vertical directions but a $T/4$ shift in time (i.e., when the atoms are rotating), where T is the period of the phonon mode (fig. S11). We continuously tuned this shift and measured the peak magnetization in comparison with the helicity of the TEFISH signal (Fig. 2B). The magnetization and helicity oscillate together, which confirms that the observed magnetization is proportional to the phonon angular momentum. The loss of helicity from the free-space THz pulses to the TEFISH signal is largely caused by the phase difference between the atomic and field contributions (*54*).

Modeling the spin and phonon dynamics

In addition, a detailed analysis of the temperature-dependent spin dynamics also validates the mechanism of phonon-induced paramagnetic relaxation. Direct pulsed THz excitation of spin-orbit transition between CEF levels should initiate constant spin polarization, but we found that the magnetization is very weak at temperatures >150 K compared with that measured at 10 K (Fig. 3A). The magnetization M is converted from the observed Kerr ellipticity with temperature- and wavelength-dependent Verdet constant (eq. S20) from literature (*56*–*58*). The greatly enhanced magnetization at cryogenic temperatures can be attributed to two factors. First, a sharper phonon resonance and longer phonon lifetime at lower temperatures lead to a larger phonon population and a stronger, longer-lasting effective magnetic field. Second, the diverging magnetic susceptibility results in more spin polarization, despite slower spin response to the field. To quantify this process, we derived the time-dependent effective magnetic field from the measured paramagnetic relaxation (*54*):

$$\frac{dM}{dt} = \frac{\chi B_{\text{eff}} - M}{\tau_{\text{spin}}} \tag{2}$$

Considering the effective magnetic field B_{eff} is short-lived, we fit τ_{spin} by the relaxation of magnetization and then calculate B_{eff} from $M(t)$ and τ_{spin}. In parallel, we solved the coherent phonon field $|Q\rangle$ as a driven mechanical oscillator by the THz field $\vec{\boldsymbol{E}}$ inside the material experienced by the phonons:

$$\frac{d^2Q}{dt^2} + \frac{1}{\tau_{\text{phonon}}}\frac{dQ}{dt} + \Omega^2 Q = \sum_i \frac{\Omega}{2\hbar}\vec{\boldsymbol{E}} \cdot \boldsymbol{e}_i^* \cdot \vec{\boldsymbol{A}}_i \tag{3}$$

where $\boldsymbol{e}_i^*$ is the Born effective charge tensor of the ith atom in the unit cell, and $\vec{\boldsymbol{A}}_i$ is the displacement in a single chiral phonon, both calculated from DFT. The effective magnetic field is then calculated from Eq. 1 by using $n = |Q|^2$ and considering the imperfect helicity of the phonons (*54*). Comparing the measured B_{eff} with that from the phonon model (Fig. 3B), we can fit the phonon lifetime. Figure 3C shows the summary of the spin and phonon lifetimes from 10 to 150 K. The spin lifetime drops from 39 ps at 10 K to 2 ps at 150 K, and the phonon lifetime decreases from 0.6 ps at 10 K to ~0.1 ps

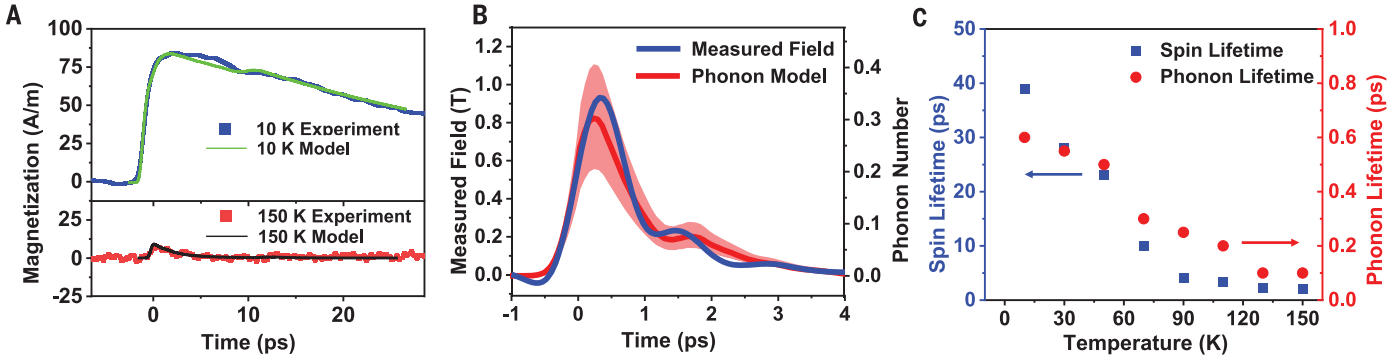

Fig. 3. The matching dynamics of magnetization and chiral phonons. (**A**) Comparing the time-resolved magnetization at 150 K, the much larger magnetization at 10 K agrees with paramagnetic relaxation in a phononic effective magnetic field and rules out direct spin excitation. (**B**) Time-dependent effective magnetic field derived from measured magnetization dynamics at 10 K aligns with that derived from phonon dynamics, using spin and phonon lifetimes as the only fitting parameters. The shadowed region indicates uncertainty from the measurement of $\Delta\Omega$. (**C**) Spin and phonon lifetimes obtained at 10 to 150 K, which reproduce the magnetization dynamics in (A) with the models of Eqs. 1 and 3.

Fig. 4. Scaling of chiral phonon–induced effective magnetic field. The experimental peak field is proportional to the incident fluence of THz excitation, as well as the peak number of chiral phonons per unit cell, as expected from theoretical Eq. 1. The shadowed region indicates uncertainty from the measurement of $\Delta\Omega$.

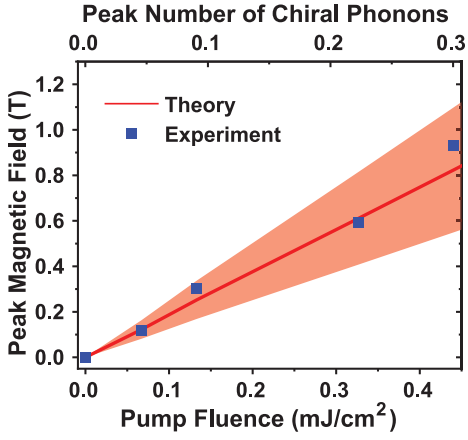

at 150 K, consistent with values obtained in similar materials (*59*). With only these two lifetimes and no free parameter to adjust the magnitude, we reproduced the magnetization throughout the temperature range (Fig. 3A and figs. S13 and S14), which validates our model of spin-phonon coupling (Eq. 1).

Finally, we verify that the effective magnetic field scales linearly with the chiral phonon population, in accordance with the symmetry requirement of spin-phonon coupling (Fig. 4). Under varying pump fluence, we measured the corresponding peak magnetization and calculated the chiral phonon population, and the slope agrees with the theoretical expectation. The maximum field strength achieved in our experiment is 0.93 T under a moderate fluence of 0.44 mJ/cm^2, corresponding to a net absorbed fluence of <0.2 mJ/cm^2 and a bond deformation of 0.7% (fig. S12). The relatively low fluence used in our experiment ensures that the magnetization is unlikely to be caused by nonlinear effects such as phonon anharmonicity or lattice-induced phase transition (*36*, *60*). The linear trend suggests that the transient effective magnetic field could approach 50 T when the absorbed fluence is >10 mJ/cm^2 (*39*, *46*), which stays below the Lindemann melting criterion and avoids significant anharmonicity (*61*).

Conclusions

We have experimentally observed the chiral phonon–induced magnetization that corresponds to effective magnetic fields on the order of 1 T in CeF_3. The magnetization of the material is controlled by the helicity of incident THz excitation and the phonons and is quantified by time-resolved magneto-optic spectroscopy. We firmly established the phononic origin of the transient magnetization by frequency- and temperature-dependent measurements, which correlate with the second-harmonic generation from the phononic structural symmetry breaking. We elucidated the pathway of angular momentum transfer from CP THz light to spins through chiral phonons and ruled out other alternative mechanisms, including the photonic inverse Faraday effects and the excitation of CEF levels. These time-resolved spin dynamics are quantitatively explained by a phenomenological spin-phonon coupling Hamiltonian and the rate equations of phonons and spins, with only two free parameters of phonon and spin lifetimes. The magnetic chiral phonons offer a new route to coherent engineering of quantum materials and THz spintronic devices.

REFERENCES AND NOTES

1. X. G. Wen, F. Wilczek, A. Zee, *Phys. Rev. B Condens. Matter* **39**, 11413–11423 (1989).
2. S. Raghu, F. D. M. Haldane, *Phys. Rev. A* **78**, 033834 (2008).
3. X.-L. Qi, S.-C. Zhang, *Rev. Mod. Phys.* **83**, 1057–1110 (2011).
4. L. Zhang, Q. Niu, *Phys. Rev. Lett.* **115**, 115502 (2015).
5. S.-W. Cheong, *Npj Quantum Mater.* **4**, 1–9 (2019).
6. R. Fleury, D. L. Sounas, C. F. Sieck, M. R. Haberman, A. Alù, *Science* **343**, 516–519 (2014).
7. J. Del Pino, J. J. Slim, E. Verhagen, *Nature* **606**, 82–87 (2022).
8. H. Zhu *et al.*, *Science* **359**, 579–582 (2018).
9. H. Chen, W. Zhang, Q. Niu, L. Zhang, *2D Mater.* **6**, 012002 (2018).
10. Z. Li *et al.*, *ACS Nano* **13**, 14107–14113 (2019).
11. E. Liu *et al.*, *Phys. Rev. Res.* **1**, 032007 (2019).
12. M. He *et al.*, *Nat. Commun.* **11**, 618 (2020).
13. D. M. Juraschek, N. A. Spaldin, *Phys. Rev. Mater.* **3**, 064405 (2019).
14. R. M. Geilhufe, V. Juričić, S. Bonetti, J.-X. Zhu, A. V. Balatsky, *Phys. Rev. Res.* **3**, L022011 (2021).
15. C. Xiao, Y. Ren, B. Xiong, *Phys. Rev. B* **103**, 115432 (2021).
16. Y. Ren, C. Xiao, D. Saparov, Q. Niu, *Phys. Rev. Lett.* **127**, 186403 (2021).
17. L.-H. Hu, J. Yu, I. Garate, C.-X. Liu, *Phys. Rev. Lett.* **127**, 125901 (2021).
18. G. Xiong, H. Chen, D. Ma, L. Zhang, *Phys. Rev. B* **106**, 144302 (2022).
19. D. Shin *et al.*, *Nat. Commun.* **9**, 638 (2018).
20. A. S. Pine, G. Dresselhaus, *Phys. Rev.* **188**, 1489–1496 (1969).
21. G. Grissonnanche *et al.*, *Nat. Phys.* **16**, 1108–1111 (2020).
22. S. G. Jeong *et al.*, *Sci. Adv.* **8**, eabm4005 (2022).
23. S. R. Tauchert *et al.*, *Nature* **602**, 73–77 (2022).
24. K. Ishito *et al.*, *Nat. Phys.* **19**, 35–39 (2022).
25. W. J. Choi *et al.*, *Nat. Photonics* **16**, 366–373 (2022).
26. K. Kim *et al.*, *Nat. Mater.* **22**, 322–328 (2023).
27. B. Koopmans *et al.*, *Nat. Mater.* **9**, 259–265 (2010).
28. G. Schaack, *Solid State Commun.* **17**, 505–509 (1975).
29. B. Cheng *et al.*, *Nano Lett.* **20**, 5991–5996 (2020).
30. A. Baydin *et al.*, *Phys. Rev. Lett.* **128**, 075901 (2022).
31. B. Flebus, A. H. MacDonald, *Phys. Rev. B* **105**, L220301 (2022).
32. X.-Q. Sun, J.-Y. Chen, S. A. Kivelson, *Phys. Rev. B* **106**, 144111 (2022).
33. R. M. Geilhufe, *Phys. Rev. Res.* **4**, L012004 (2022).
34. S. Chaudhary, D. M. Juraschek, M. Rodriguez-Vega, G. A. Fiete, arXiv.2306.11630 (2023).

35. D. M. Juraschek, T. Neuman, P. Narang, *Phys. Rev. Res.* **4**, 013129 (2022).
36. M. Först *et al*., *Nat. Phys.* **7**, 854–856 (2011).
37. B. Liu *et al*., *Phys. Rev. X* **10**, 011053 (2020).
38. A. S. Disa, T. F. Nova, A. Cavalleri, *Nat. Phys.* **17**, 1087–1092 (2021).
39. A. S. Disa *et al*., *Nat. Phys.* **16**, 937–941 (2020).
40. A. Stupakiewicz *et al*., *Nat. Phys.* **17**, 489–492 (2021).
41. T. F. Nova *et al*., *Nat. Phys.* **13**, 132–136 (2017).
42. D. Afanasiev *et al*., *Nat. Mater.* **20**, 607–611 (2021).
43. D. N. Basov, R. D. Averitt, D. Hsieh, *Nat. Mater.* **16**, 1077–1088 (2017).
44. M. Basini *et al*. arXiv:2210.01690 (4 October 2022).
45. C. S. Davies, N. Fennema, A. Tsukamoto, A. Kirilyuk, "Ultrafast Helicity-Dependent Magnetic Switching by Optical Phonons Driven at Resonance" in *2022 47th International Conference on Infrared, Millimeter and Terahertz Waves (IRMMW-THz)* (2022), p. 1.
46. M. Seo, J.-H. Mun, J. Heo, D. E. Kim, *Sci. Rep.* **12**, 16273 (2022).
47. G. Schaack, *J. Phys. C Solid State Phys.* **9**, L297–L301 (1976).
48. G. Schaack, *Physica B+C* **89**, 195–200 (1977).
49. H. Gerlinger, G. Schaack, *J. Phys. Colloq.* **42**, C6-499, C6–C501 (1981).
50. J. M. Baker, R. S. Rubins, Electron Spin Resonance in Two Groups of Lanthanon Salts, *Proc. Phys. Soc.* **78**, 1353–1360 (1961).
51. R. P. Leavitt, C. A. Morrison, *J. Chem. Phys.* **73**, 749–757 (1980).
52. H. Gerlinger, G. Schaack, *Phys. Rev. B Condens. Matter* **33**, 7438–7450 (1986).
53. P. Thalmeier, P. Fulde, *Z. Phys. B Condens. Matter Quanta* **26**, 323–328 (1977).
54. Materials, methods, and additional information are available in the supplementary materials.
55. T. Lin *et al*., Optica Open [Preprint] (2023); https://doi.org/10.1364/opticaopen.22066295.v2.
56. C. Leycuras, H. Le Gall, M. Guillot, A. Marchand, *J. Appl. Phys.* **55**, 2161–2163 (1984).
57. L. Gong-qiang, Z. Wen-kang, Z. Xing, *Phys. Rev. B Condens. Matter* **48**, 16091–16094 (1993).
58. D. Vojna *et al*., *Opt. Eng.* **56**, 067105 (2017).
59. R. Kolesov *et al*., *Phys. Rev. Lett.* **111**, 120502 (2013).
60. A. Subedi, A. Cavalleri, A. Georges, *Phys. Rev. B Condens. Matter Mater. Phys.* **89**, 220301 (2014).
61. A. von Hoegen, R. Mankowsky, M. Fechner, M. Först, A. Cavalleri, *Nature* **555**, 79–82 (2018).

ACKNOWLEDGMENTS

We thank A. Donohue from J.A. Woollam Co., Inc., for assistance in measuring the dielectric function of the CeF_3 crystal. We also thank D. Juraschek (Tel Aviv University) and S. Zollner (New Mexico State University) for helpful discussions. **Funding:** National Science Foundation grants DMR-2005096 (J.L., X.C., and H.Z.), 1842494 (E.R.B.), and DMR-2240106 (H.Z.); Welch Foundation grant C-2128 (R.X., T.L., and H.Z.); Army Research Office grant W911NF-16-1-0255 (J.Z. and B.I.Y.); and Office of Naval Research grant N00014-22-1-2753 (J.Z. and B.I.Y.). **Author contributions:** Conceptualization: H.Z.; Methodology: J.L., X.C., and H.Z.; Investigation: J.L., T.L., J.Z., and H.Z.; Validation: J.L. and H.Z.; Visualization: J.L., E.R.B., R.X., and H.Z.; Funding acquisition: H.Z. and B.I.Y.; Writing: J.L., T.L., J.Z., X.C., E.R.B., R.X., B.I.Y., and H.Z. **Competing interests:** The authors declare no competing interests. **Data and materials availability:** All data needed to evaluate the conclusions are available in the main text or the supplementary materials.

SUPPLEMENTARY MATERIALS

science.org/doi/10.1126/science.adi9601
Materials and Methods
Supplementary Text
Figs. S1 to S14
Tables S1 and S2
References (*62*–*76*)

Submitted 1 June 2023; accepted 7 September 2023
10.1126/science.adi9601